In Situ Formation of an Oxygen-Evolving Catalyst in Neutral Water Containing Phosphate and Co 2+

Matthew W. Kanan, *et al.*

Science **321**, 1072 (2008);
DOI: 10.1126/science.1162018

In Situ Formation of an Oxygen-Evolving Catalyst in Neutral Water Containing Phosphate and Co^{2+}

Matthew W. Kanan and Daniel G. Nocera*

The utilization of solar energy on a large scale requires its storage. In natural photosynthesis, energy from sunlight is used to rearrange the bonds of water to oxygen and hydrogen equivalents. The realization of artificial systems that perform "water splitting" requires catalysts that produce oxygen from water without the need for excessive driving potentials.
Here we report such a catalyst that forms upon the oxidative polarization of an inert indium tin oxide electrode in phosphate-buffered water containing cobalt (II) ions. A variety of analytical techniques indicates the presence of phosphate in an approximate 1:2 ratio with cobalt in this material. The pH dependence of the catalytic activity also implicates the hydrogen phosphate ion as the proton acceptor in the oxygen-producing reaction. This catalyst not only forms in situ from earth-abundant materials but also operates in neutral water under ambient conditions.

Sunlight is the only renewable and carbon-neutral energy source of sufficient scale to replace fossil fuels and meet rising global energy demand (*1*). The diurnal variation in local insolation, however, demands a cost-effective storage of solar energy for its large-scale utilization. Of the possible storage methods, nature provides the blueprint for storing sunlight in the form of chemical fuels (*1*, *2*). The primary steps of natural photosynthesis involve the absorption of sunlight and its conversion into spatially separated electron/hole pairs. The holes of this wireless current are then captured by the oxygen-evolving complex (OEC) to oxidize water to oxygen and the electrons are captured by photosystem I to reduce $NADP^+$ (nicotinamide adenine dinucleotide phosphate) to NADPH (the reduced form of $NADP^+$), nature's form of hydrogen (*3*). Thus, the overall primary events of photosynthesis store solar energy in a fuel by rearranging the chemical bonds of water to form H_2 (i.e., NADPH) and O_2.

An approach to duplicating photosynthesis outside of a photosynthetic membrane is to convert sunlight into spatially separated electron/hole pairs within a photovoltaic cell and then capture the charges with catalysts that mediate "water splitting" (*1*, *4*). The four holes are captured by a catalyst at the anode to produce oxygen, and the four electrons are captured by a separate catalyst at the cathode to produce hydrogen. The net result is the storage of solar energy in the chemical bonds of H_2 and O_2.

A key determinant of energy storage in artificial photosynthesis is the efficiency of the water-splitting catalysts. Electrocatalysts that are efficient for solar-to-fuels conversion must operate close to the Nernstian potentials (E) for the H_2O/O_2 and H_2O/H_2 half-cell reactions shown in Scheme 1 (half-cell potentials given in the convention of reduction potentials).

The voltage in addition to E that is required to attain a given catalytic activity—referred to as overpotential—limits the efficiency of converting light into catalytic current. Of the two reactions, the H_2O/O_2 reaction is considerably more complex (*5*). This reaction requires a four-electron oxidation of two water molecules coupled to the removal of four protons to form a relatively weak oxygen-oxygen bond. In addition to controlling this proton-coupled electron transfer (PCET) (*6*, *7*), a catalyst must tolerate prolonged exposure to oxidizing conditions. Even at the thermodynamic limit, water oxidation requires an oxidizing power that causes most chemical functional groups to degrade. Accordingly, the generation of oxygen from water presents a substantial challenge toward realizing artificial photosynthesis (*8*).

The fine-tuned molecular machinery of the OEC oxidizes water at a low overpotential using a Mn_4O_4Ca cluster (*9*–*12*). Outside the OEC, examples of water oxidation catalysts include first-row spinel and perovskite metal oxides, which require concentrated basic solutions (pH > 13) and moderate overpotentials (<400 mV), and precious metals and precious metal oxides, which operate with similar efficiencies under acidic conditions (pH < 1) (*13*–*15*). However, few catalysts operate in neutral water under ambient conditions. Neutral water is oxidized at Pt electrodes, and some precious metal oxides have been reported to operate electrocatalytically in neutral or weakly acidic solutions (*16*). The development of an earth-abundant, first-row catalyst that operates at pH 7 at low overpotential remains a fundamental chemical challenge. Here, we report an oxygen-evolving catalyst that forms in situ upon anodic polarization of an inert electrode in neutral aqueous phosphate solutions containing Co^{2+}. Oxygen generation occurs under benign conditions: pH = 7, 1 atm, and room temperature.

Cobalt ions in the presence of chemical oxidants such as $Ru(bpy)_3^{3+}$ (bpy, bipyridine; E^o = 1.26, where E^o is the standard potential) catalyze the oxidation of water to O_2 in neutral phosphate solutions (*17*, *18*). Oxygen yields drop in these reactions when oxidized Co species precipitate from solution because the catalytically active species is removed from the solution-phase reaction. However, an oxidation-induced precipita-

$$O_2 + 4H^+ + 4e^- \rightleftharpoons 2H_2O \qquad E_{anodic} = 1.23\,V - 0.059\,(pH)\,V \text{ vs NHE}$$

$$4H^+ + 4e^- \rightleftharpoons 2H_2 \qquad E_{cathodic} = 0\,V - 0.059\,(pH)\,V \text{ vs NHE}$$

$$2H_2O \longrightarrow 2H_2 + O_2 \qquad E_{rxn} = -1.23\,V$$

Scheme 1.

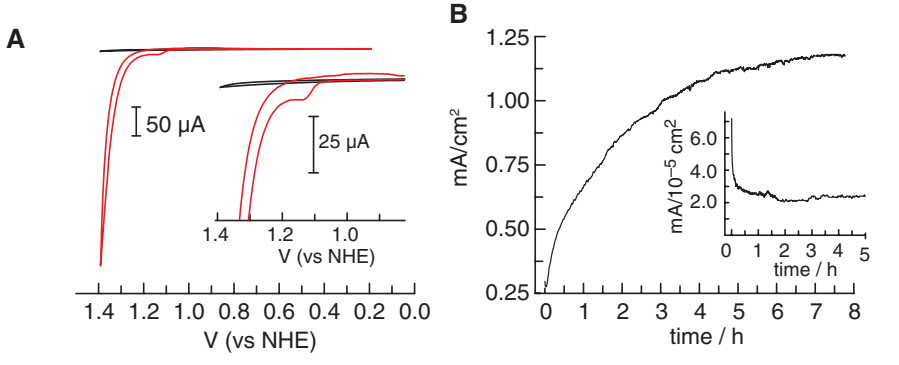

Fig. 1. (**A**) Cyclic voltammagram in 0.1 M KPi electrolyte at pH 7.0 with no Co^{2+} ion present (black line) and with 0.5 mM Co^{2+} present (red line). The potential was measured against a Ag/AgCl reference and converted to NHE potentials by using E(NHE) = E(Ag/AgCl) + 0.197 V. (**B**) Current density profile for bulk electrolysis at 1.29 V (versus NHE) in 0.1 M KPi electrolyte at pH 7.0 containing 0.5 mM Co^{2+}. (Inset) Profile in the absence of Co^{2+}.

Department of Chemistry, 6-335, Massachusetts Institute of Technology, Cambridge, MA 02139–4307, USA.

*To whom correspondence should be addressed. E-mail: nocera@mit.edu

tion may be exploited to prepare electrocatalysts in situ if the precipitated material remains catalytically active and can be oxidized at an electrode surface. To explore this possibility for Co-catalyzed water oxidation, we examined electrochemical oxidations of aqueous solutions containing phosphate and Co^{2+}. Cyclic voltammetry of a 0.5 mM solution of $Co(NO_3)_2$ in 0.1 M potassium phosphate pH 7.0 (KPi electrolyte) exhibits an oxidation wave at $E_p = 1.13$ V (where E_p is the peak potential) versus the normal hydrogen electrode (NHE), followed by the onset of a strong catalytic wave at 1.23 V (Fig. 1A). A broad, relatively weak reduction wave is observed on the cathodic scan. The presence of a catalytic wave prompted us to examine the electrode activity during controlled-potential electrolysis.

Indium tin oxide (ITO) was used as the electrode for bulk electrolysis to ensure a minimal background activity for O_2 production. An electrolysis at 1.29 V without stirring in neutral KPi electrolyte containing 0.5 mM Co^{2+} exhibits a rising current density that reaches a peak value >1 mA/cm^2 after 7 to 8 hours (Fig. 1B). During this time, a dark coating forms on the ITO surface, and effervescence from this coating becomes increasingly vigorous (*19*).The same results are observed with either $CoSO_4$, $Co(NO_3)_2$, or $Co(OTf)_2$ (where OTf = triflate) as the Co^{2+} source, which indicates that the original Co^{2+} counterion is unimportant and that this activity does not depend on an impurity found in a specific source. The amount of charge passed during the course of an 8-hour electrolysis far exceeds what could be accounted for by stoichiometric oxidation of the Co^{2+} in solution (*20*). These observations are indicative of the in situ formation of an oxygen-evolving catalyst. Catalyst formation also proceeds on a fluorine tin oxide electrode and if KPi is replaced by NaPi electrolyte. In a control experiment, the current density during bulk electrolysis under identical conditions in the absence of Co^{2+} rapidly drops to a baseline level of ~25 nA/cm^2 (inset in Fig. 1B).

The morphology of the electrode coating formed during electrolysis in the presence of Co^{2+} was examined by scanning electron microscopy (SEM). The electrodeposited material consists of particles that have coalesced into a thin film and individual micrometer-sized particles on top of the film (Fig. 2A). The ITO substrate can be seen through cracks in the film that form upon drying, as evidenced by particles that are split into complementary pieces. The film thickness gradually increases over the course of the electrodeposition (see fig. S4 for additional images). At maximum activity under these electrolysis conditions, the film is >2 μm thick. The x-ray powder diffraction pattern of an electrodeposited catalyst shows broad amorphous features and no peaks indicative of crystalline phases other than the peaks associated with the ITO layer (fig. S1).

In the absence of detectable crystallites, the composition of the electrodeposited material was analyzed by three complementary techniques. Energy-dispersive x-ray analysis (EDX) spectra were obtained from multiple 100-to-300–m^2 regions of several independently prepared samples. These spectra identify Co, P, K, and O as the principal elemental components of the material (Fig. 2B). Although the material's morphology is not ideally suited for quantitative EDX, the analyses consistently indicate a Co:P:K ratio between ~2:1:1 and 3:1:1. To obtain an independent determination of elemental composition, electrolysis was performed with several larger ITO electrodes; the deposited material was scraped off and combined for a total yield of ~3 mg. Microanalytical elemental analysis of the combined material indicates 31.1% Co, 7.70% P, and 7.71% K, corresponding to a 2.1:1.0:0.8 Co:P:K ratio. Finally, the surface of an electrodeposited catalyst on the ITO substrate was analyzed by x-ray photoelectron spectroscopy (XPS). All peaks in the XPS spectra are accounted for by the elements detected above, in addition to In and Sn from the ITO substrate. The high-resolution P 2p peak at 133.1 eV is consistent with phosphate. The Co 2p peaks at 780.7 and 795.7 eV are in a range typical of Co^{2+} or Co^{3+} bound to oxygen (fig. S2) (*21*). Together, the x-ray diffraction and analytical results indicate that electrolysis of a Co^{2+} solution in neutral KPi electrolyte results in the electrodeposition of an amorphous Co oxide or hydroxide incorporating a substantial amount of phosphate anion at a stoichiometric ratio of roughly 2:1:1 for Co:P:K.

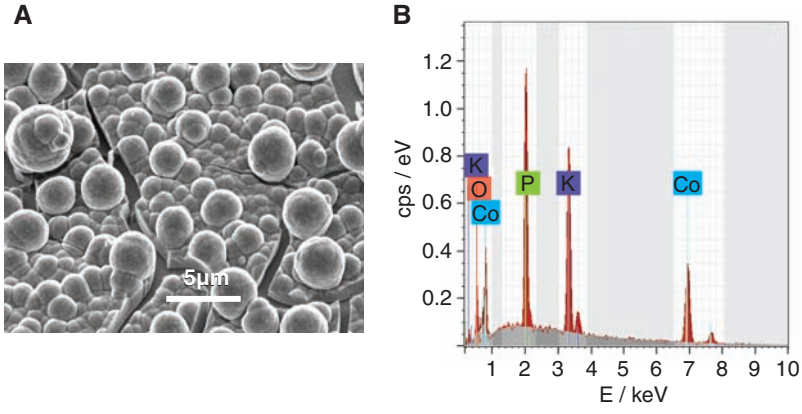

Fig. 2. (**A**) SEM image (30° tilt) of the electrodeposited catalyst after 30 C/cm^2 were passed in 0.1 M KPi electrolyte at pH 7.0, containing 0.5 mM Co^{2+}. The ITO substrate can be seen through cracks in the dried film. (**B**) Typical EDX histogram acquired at 12 kV. cps, counts per second.

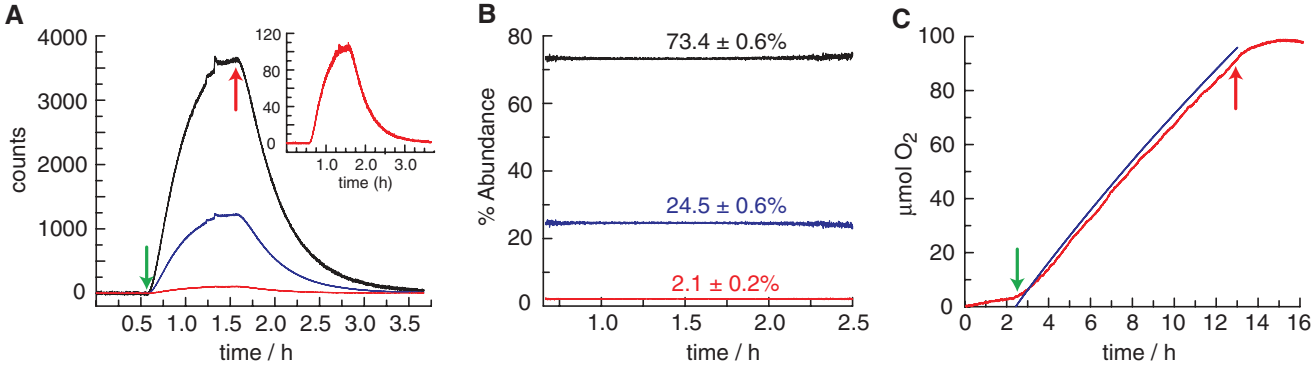

Fig. 3. (**A**) Mass spectrometric detection of isotopically labeled $^{16,16}O_2$ (black line), $^{16,18}O_2$ (blue line), and $^{18,18}O_2$ (red line) during electrolysis of a catalyst film on ITO in a KPi electrolyte containing 14.6% $^{18}OH_2$. The green arrow indicates the initiation of electrolysis at 1.29 V (NHE), and the red arrow indicates the termination of electrolysis. (Inset) Expansion of the $^{18,18}O_2$ signal. (**B**) Percent abundance of each isotope over the course of the experiment. Average observed abundance of ±2σ is indicated above each line. Statistical abundances are 72.9, 24.9, and 2.1%. (**C**) O_2 production measured by fluorescent sensor (red line) and theoretical amount of O_2 produced (blue line), assuming a Faradic efficiency of 100%. The green arrow indicates the initiation of electrolysis at 1.29 V, and the red arrow indicates the termination of electrolysis.

Three experiments were performed to establish that the catalytic activity observed with this material corresponds to authentic water oxidation. Each of these experiments was performed in neutral KPi electrolyte in the absence of Co^{2+}. Catalyst coatings (~1.3 cm^2) were prepared in a preliminary step as described above and stored under ambient laboratory conditions until they were used.

To confirm that water is the source of the O_2 produced, electrolysis was performed in helium-saturated electrolyte containing 14.6% $^{18}OH_2$ in a gas-tight electrochemical cell in line with a mass spectrometer. The helium carrier gas was continuously flowed through the headspace of the anodic compartment into the mass spectrometer, and the relative abundances of $^{32}O_2$, $^{34}O_2$, and $^{36}O_2$ were monitored at 2-s intervals. Within minutes of initiating electrolysis at 1.29 V, the signals for the three isotopes began to rise above their background levels as the O_2 produced by the catalyst escaped into the headspace. Upon terminating the electrolysis 1 hour later, these signals slowly returned to their background levels (Fig. 3A). The $^{32}O_2$, $^{34}O_2$, and $^{36}O_2$ isotopes were detected in the statistical ratio (72.9, 24.9, and 2.1% relative abundances, respectively) (Fig. 3B).

The Faradaic efficiency of the catalyst was measured with a fluorescence-based O_2 sensor. Electrolysis was performed in KPi electrolyte in a gas-tight electrochemical cell under an N_2 atmosphere with the sensor placed in the headspace. After initiating electrolysis at 1.29 V, the percentage of O_2 detected in the headspace rose in accord with what was predicted by assuming that all of the current was caused by $4e^-$ oxidation of water to produce O_2 (Fig. 3C). The amount of O_2 produced (95 μmol, 3.0 mg) greatly exceeds the amount of catalyst (~0.2 mg), which shows no perceptible decomposition during the course of the experiment.

The stability of phosphate under catalytic conditions was assayed by ^{31}P nuclear magnetic resonance (NMR). Electrolysis in a two-compartment cell with 10 mL of KPi electrolyte (1 mmol phosphate) on each side was allowed to proceed until 45 C had been passed through the cell (0.46 mmol electrons). Electrolysis solutions from both chambers show single, clean ^{31}P resonances, which indicate that the electrolyte is robust under these conditions (fig. S3). Together, the mass spectrometry, Faradaic efficiency, and ^{31}P NMR results demonstrate that the electrodeposited catalyst cleanly oxidizes H_2O to O_2 in neutral KPi solutions.

The current density of a catalyst on ITO was measured as a function of the overpotential (η) in KPi electrolyte without Co^{2+} (black circles in Fig. 4A). At pH 7.0, appreciable catalytic current is observed beginning at η = 0.28 V, and a current density of 1 mA/cm^2 (corresponding to 9 μmol O_2 cm^{-2} h^{-1}) requires η = 0.41 V. The Tafel plot deviates slightly from linearity, possibly reflecting an uncompensated iR drop caused by the surface resistivity of the ITO (8 to 12 ohms per square). Substantial improvements in the activity profile may be attainable without changing the catalyst composition by depositing on alternative substrates or improving ohmic contact to the ITO.

The catalyst used to obtain the Tafel plot at pH 7 was subsequently transferred to KPi electrolyte at pH 4.6, and the current density was measured at a constant applied potential (1.24 V) while the pH was increased incrementally to 9.4 by adding aliquots of concentrated KOH. A plot of the log of current density versus pH exhibits a steep initial rise that levels off in the high-pH range such that increasing the pH from 8 to 9.4 at this applied potential has little effect (Fig. 4B). These data can be converted to a Tafel plot by using Eq. 1 (Scheme 1) and accounting for iR drop (see Fig. 4 legend). A comparison to the Tafel plot obtained at pH 7 indicates that the catalyst exhibits approximately Nernstian behavior from pH 5 to 8: Increasing the pH by one unit at constant applied potential (1.24 V) has nearly the same effect as increasing the overpotential by 0.059 V at pH 7 (red circles in Fig. 4A). This result implicates a reversible ne^-, nH^+ removal before the rate-determining step for O_2 evolution in this pH range (here, n is the number of equivalents). Thus, an important component of the activity at pH 7 with this catalyst is the existence of one or more intermediates preceding O_2 formation that are deprotonated reversibly by HPO_4^{2-} in a PCET event (*22*). The pH-independent behavior above pH 8 at the applied potential may indicate a change in mechanism, most likely involving a deprotonated intermediate.

In addition to mediating the deprotonation required for catalysis, the KPi electrolyte provides a medium for in situ catalyst formation. Given that phosphate is a structural element and that the catalyst forms under oxidizing conditions, it is plausible that deposition is driven by the interaction of phosphate and Co^{3+}. By judicious choice of other metal-anion pairs or combinations of multiple metals and anions, it may be possible to access other oxygen-evolving catalysts that form in situ and operate in neutral solutions. In situ formation is advantageous because, in principle, it enables catalyst deposition on a variety of substrates, including those that are too delicate to tolerate traditional catalyst preparation techniques. This attribute is important for interfacing a catalyst with a variety of electrochemical or photoelectrochemical cell designs.

In situ formation also implies a self-repair mechanism. Proposed molecular mechanisms involving O_2/H_2O cycles at Co centers suggest that catalytic reactions cycle among Co^{2+}-, Co^{3+}-, and Co^{4+}-oxo oxidation states (*18*, *23*). The propensity of metal ion dissolution has been shown to correlate with ligand substitution (*24*). Given that Co^{3+} is substitutionally inert relative to Co^{2+}, a dynamic equilibrium between Co^{2+}-HPO_4^{2-} in solution and Co^{3+}-HPO_4^{2-} on the anodically poised electrode may be established. More generally, if a catalytic cycle involves an oxidation state that is prone to dissolution, this process can be countered by continual catalyst formation by establishing an equilibrium with the judicious choice of an anion.

The results reported herein highlight a new area of exploration for the development of easily prepared, earth-abundant catalysts that oxidize water. If artificial photosynthesis is to enable the storage of solar energy commensurate with global demand, water-splitting chemistry will need to be performed at a daunting scale. Storing the equivalent of the current energy demand would require splitting more than 10^{15} mol/year of water, which is roughly 100 times the scale of nitrogen fixation by the Haber-Bosch process. The conditions under which water splitting is performed will determine how solar energy is deployed. The catalyst reported here has many elements of natural photosynthesis, including (i) its formation from earth-abundant metal ions in aqueous solution, (ii) a plausible pathway for self-repair, (iii) a carrier for protons in neutral water, and (iv) the generation of O_2 at low overpotential, neutral pH, 1 atm, and room temperature.

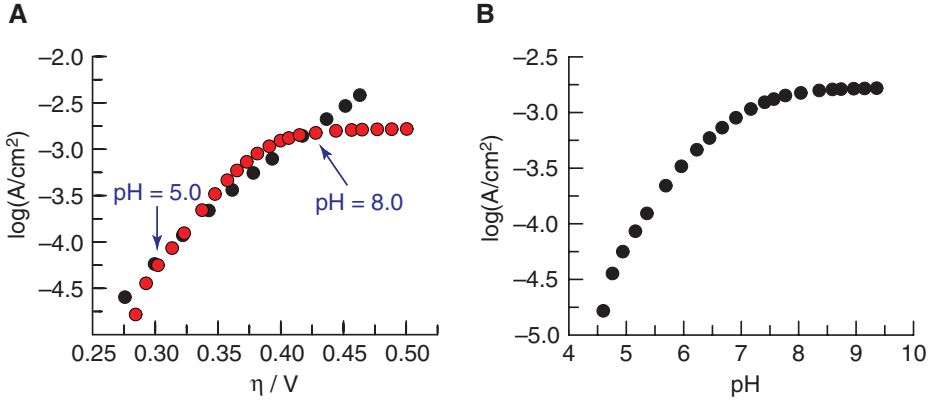

Fig. 4. (**A**) Tafel plot (black circles), $\eta = (V_{appl} - iR) - E(pH\ 7)$ (where V_{appl} is the applied potential), of a catalyst film on ITO in 0.1 M KPi electrolyte pH 7.0, corrected for the iR drop of the solution. pH data were converted into a Tafel plot (red circles), $\eta = (V_{appl} + 0.059\Delta pH - iR) - E(pH\ 7)$, assuming Nernstian behavior and correcting for the iR drop of the solution. The pH = 5 and pH = 8 data points are indicated by arrows. (**B**) Current density dependence on pH in 0.1 M KPi electrolyte. The potential was set at 1.24 V (versus NHE) with no iR compensation.

References and Notes

1. N. S. Lewis, D. G. Nocera, *Proc. Natl. Acad. Sci. U.S.A.* **103**, 15729 (2006).
2. N. Nelson, A. Ben-Shem, *Nat. Rev. Mol. Cell Biol.* **5**, 971 (2004).
3. J. Barber, *Philos. Trans. R. Soc. London Ser. A* **365**, 1007 (2007).
4. A. J. Bard, M. A. Fox, *Acc. Chem. Res.* **28**, 141 (1995).
5. T. A. Betley, Q. Wu, T. Van Voorhis, D. G. Nocera, *Inorg. Chem.* **47**, 1849 (2008).
6. R. I. Cukier, D. G. Nocera, *Annu. Rev. Phys. Chem.* **49**, 337 (1998).
7. M. H. V. Huynh, T. J. Meyer, *Chem. Rev.* **107**, 5004 (2007).
8. R. Eisenberg, H. B. Gray, *Inorg. Chem.* **47**, 1697 (2008).
9. K. N. Ferreira, T. M. Iverson, K. Maghlaoui, J. Barber, S. Iwata, *Science* **303**, 1831 (2004), published online 5 February 2004; 10.1126/science.1093087.
10. S. Iwata, J. Barber, *Curr. Opin. Struct. Biol.* **14**, 447 (2004).
11. J. Yano *et al.*, *Science* **314**, 821 (2006).
12. B. Loll, J. Kern, W. Saenger, A. Zouni, J. Biesiadka, *Nature* **438**, 1040 (2005).
13. S. Trassati, in *Electrochemistry of Novel Materials*, J. Lipkowski, P. N. Ross, Eds. (VCH, New York, 1994), chap. 5.
14. J. O. Bockris, T. J. Otagawa, *J. Electrochem. Soc.* **131**, 290 (1984).
15. M. R. Tarasevich, B. N. Efremov, in *Electrodes of Conductive Metal Oxides*, S. Trasatti, Ed. (Elsevier, Amsterdam, 1980), chap. 5.
16. M. Yagi, E. Tomita, S. Sakita, T. Kuwabara, K. Nagai, *J. Phys. Chem. B* **109**, 21489 (2005).
17. V. Y. Shafirovich, N. K. Khannanov, V. V. Strelets, *Nouv. J. Chim.* **4**, 81 (1980).
18. B. S. Brunschwig, M. H. Chou, C. Creutz, P. Ghosh, N. Sutin, *J. Am. Chem. Soc.* **105**, 4832 (1983).
19. Materials and methods, videos of an active electrode, and figs. S1 to S4 are available as supporting material on *Science* Online.
20. In a typical experiment, >40 C are passed over 8 hours, whereas oxidation of all the Co^{2+} in solution requires 1.9 C per oxidation-state change.
21. K. D. Bomben, J. F. Moulder, P. E. Sobol, W. F. Stickel, in *Handbook of X-Ray Photoelectron Spectra: A Reference Book of Standard Spectra for Identification*, J. Chastain, Ed. (Perkin Elmer, Eden Prairie, MN, 1992).
22. T. Irebo, S. Y. Reece, M. Sjödin, D. G. Nocera, L. Hammarström, *J. Am. Chem. Soc.* **129**, 15462 (2007).
23. C. J. Chang, Z.-H. Loh, C. Shi, F. C. Anson, D. G. Nocera, *J. Am. Chem. Soc.* **126**, 10013 (2004).
24. W. H. Casey, *J. Colloid Interface Sci.* **146**, 586 (1991).

25. This work was supported by a grant from the NSF Chemical Bonding Center (CHE-0802907). M.W.K. is supported by a Ruth L. Kirchenstein National Research Service Award postdoctoral fellowship provided by NIH (F32GM07782903). We thank E. Shaw for obtaining XPS spectra, G. Henoch for providing the videos in the supporting online material, and Y. Surendranath for many productive discussions.

Supporting Online Material

www.sciencemag.org/cgi/content/full/1162018/DC1
Materials and Methods
Figs. S1 to S4
Movies S1 and S2

19 June 2008; accepted 18 July 2008
Published online 31 July 2008;
10.1126/science.1162018
Include this information when citing this paper.

The Global Atmospheric Circulation on Moist Isentropes

Olivier Pauluis,[1]* Arnaud Czaja,[2] Robert Korty[3]

The global atmospheric circulation transports energy from the equatorial regions to higher latitudes through a poleward flow of high-energy and -entropy parcels and an equatorward flow of air with lower energy and entropy content. Because of its turbulent nature, this circulation can only be described in some averaged sense. Here, we show that the total mass transport by the circulation is twice as large when averaged on moist isentropes than when averaged on dry isentropes. The additional mass transport on moist isentropes corresponds to a poleward flow of warm moist air near Earth's surface that rises into the upper troposphere within mid-latitudes and accounts for up to half of the air in the upper troposphere in polar regions.

Earth absorbs shortwave radiation from the Sun and emits back longwave radiation to space. Although the total amounts of energy received and emitted are about equal, Earth absorbs more energy than it emits in the equatorial regions and emits more energy than it absorbs at high latitudes (*1*). Such imbalance requires an energy transport by the atmosphere and the oceans, with the former responsible for the bulk of the transport in mid-latitudes (*2*). Determining the relationship between the atmospheric energy transport and the global distribution of temperature and humidity is a central question for our understanding of the Earth's climate.

Averaging the global atmospheric circulation usually implies computing a zonal and temporal mean over a sufficiently long period. One of the most common descriptions is the Eulerian mean circulation (*1*), obtained by averaging the flow at constant pressure or geopotential height. The Eulerian mean stream function Ψ_p is defined as

$$\Psi_p(p,\phi) = \frac{1}{\tau}\int_0^{\tau}\int_0^{2\pi}\int_p^{p_{\mathrm{surf}}} va\cos\phi\frac{dp}{g}d\lambda dt \qquad (1)$$

Here, p is pressure, ϕ is latitude, τ is the time period over which the average is computed, p_{surf} is surface pressure, λ is longitude, a is Earth's radius, v is the meridional velocity, and g is the gravitational acceleration. Figure 1A shows the annual mean stream function on pressure surfaces based on the National Centers for Environmental Prediction–National Center for Atmospheric Research (NCEP-NCAR) Reanalysis monthly data (*3*) from January 1970 to December 2004. The Eulerian-mean circulation exhibits a three-cell structure in each hemisphere: the Hadley cell in the tropics, the Ferrel cell in mid-latitudes, and a polar cell at high latitudes. The Hadley and polar cells, with air parcels moving poleward at high altitude and equatorward at low altitude, are direct circulations that transport energy toward the poles. In the Ferrel cell, the flow is poleward near the surface and equatorward at high altitude. This corresponds to an energy transport toward the equator. Nonetheless, in mid-latitudes, synoptic-scale (~1000 km) eddies transport more energy toward the poles than is brought equatorward by the Ferrel cell, so that the total energy transport in the atmosphere remains poleward.

An alternative to the Eulerian mean circulation is to average the circulation on isentropic surfaces (*4*–*6*). In atmospheric sciences, it is common to use the potential temperature θ instead of entropy. The potential temperature is given by $\theta = \left(\frac{p_0}{p}\right)^{\frac{R}{C_p}} T$, with p the pressure, R the ideal gas constant, C_p the specific heat, T the temperature, and $p_0 = 1000$ mbar an arbitrary reference pressure. Potential temperature is conserved for reversible adiabatic transformations in the absence of a phase transition, and a surface of constant potential temperature corresponds to isentropic surfaces. The stream function $\Psi_\theta(\theta,\phi)$ on potential temperature surfaces is defined by

$$\Psi_\theta(\theta_0,\phi) = \frac{1}{\tau}\int_0^{\tau}\int_0^{2\pi}\int_0^{p_{\mathrm{surf}}} H(\theta_0-\theta)va\cos\phi\frac{dp}{g}d\lambda dt \qquad (2)$$

Here, $H(x)$ is the Heavyside function, with $H(x) = 1$ for $x \geq 0$ and $H(x) = 0$ for $x < 0$. Figure 1B shows the annual mean stream function on potential temperature surfaces based on the NCEP-NCAR Reanalysis daily data from January 1970 to December 2004.

In contrast to the Eulerian mean circulation, the circulation in isentropic coordinates exhibits a single overturning cell in each hemisphere. Because the atmosphere is stratified in potential temperature ($\partial_z\theta > 0$), the isentropic circulation corresponds to a poleward flow at upper levels balanced by a return flow near Earth's surface—in the direction opposite to the Eulerian mean circulation (*4*). The meridional mass transport on an isentrope can be written as

$$\overline{\rho_\theta v} = \overline{\rho}_\theta\overline{v} + \overline{\rho_\theta' v'} \qquad (3)$$

[1]Courant Institute of Mathematical Sciences, New York University, 251 Mercer Street, New York, NY 10012, USA. [2]Space and Atmospheric Physics Group, Department of Physics, Imperial College, Huxley Building, Room 726, London SW7 2AZ, UK. [3]Department of Atmospheric Sciences, Texas A&M University, 3150 TAMU, College Station, TX 77843–3150, USA.

*To whom correspondence should be addressed. E-mail: pauluis@cims.nyu.edu